

Detection Schemes with Low-Resolution ADCs and Spatial Oversampling for Transmission with Higher-Order Constellations in the Terahertz Band

Christian Forsch, *Graduate Student Member, IEEE*, Peter Zillmann, Osama Alrabadi, Stefan Brueck, and Wolfgang Gerstacker, *Senior Member, IEEE*

Abstract—In this work, we consider Terahertz (THz) communications with low-resolution uniform quantization and spatial oversampling at the receiver side. We compare different analog-to-digital converter (ADC) parametrizations in a fair manner by keeping the ADC power consumption constant. Here, 1-, 2-, and 3-bit quantization is investigated with different oversampling factors. We analytically compute the statistics of the detection variable, and we propose the optimal as well as several suboptimal detection schemes for arbitrary quantization resolutions. Then, we evaluate the symbol error rate (SER) of the different detectors for a 16- and a 64-ary quadrature amplitude modulation (QAM) constellation. The results indicate that there is a noticeable performance degradation of the suboptimal detection schemes compared to the optimal scheme when the constellation size is larger than the number of quantization levels. Furthermore, at low signal-to-noise ratios (SNRs), 1-bit quantization outperforms 2- and 3-bit quantization, respectively, even when employing higher-order constellations. We confirm our analytical results by Monte Carlo simulations. Both a pure line-of-sight (LoS) and a more realistically modeled indoor THz channel are considered. Then, we optimize the input signal constellation with respect to SER for 1-bit quantization. The results show that the minimum SER can be lowered significantly for 16-QAM by increasing the distance between the inner and outer points of the input constellation. For larger constellations, however, the achievable reduction of the minimum SER is much smaller compared to 16-QAM.

Index Terms—Low-resolution quantization, oversampling, Terahertz communications, maximum-likelihood detection, symbol error rate, constellation optimization.

I. INTRODUCTION

FUTURE wireless communication systems are expected to provide ultra-high data rates with extremely low latency in order to enable a plethora of new applications [2]. The large bandwidths and high symbol rates which are required for such applications and which can be realized in the Terahertz (THz) band necessitate very high sampling frequencies of analog-to-digital converters (ADCs), causing a high power consumption. This problem can be tackled by decreasing the quantization

resolution of the ADC [3], arriving at low-resolution quantization such as 1-, 2-, or 3-bit quantization. However, such quantization with only few bit limits the spectral efficiency to 1-3 bit per channel use (bpcu) per real dimension for Nyquist-rate sampling [4]. Oversampling provides a remedy to increase the achievable rate by retrieving some of the information lost due to quantization [5]–[8]. This can be achieved in the temporal domain by increasing the sampling frequency or in the spatial domain by receiving the useful signal via multiple antennas/channels. Therefore, in this work, we consider the case of low-resolution quantization with spatial oversampling at the receiver side. Furthermore, we focus on higher-order constellations, implying that the number of quantization intervals of the ADC is typically smaller than the number of possible transmit symbols in our scenarios.

Communication systems with oversampled low-resolution quantization have been already previously studied in the literature. In particular, the case of 1-bit quantization was considered frequently in previous works due to its relevance and simplicity. In [9], a spread spectrum system with 1-bit quantization was considered which has similarities to our system model. It was shown that binary phase-shift keying (PSK) is not optimal anymore with respect to the channel capacity when observing the transmitted symbol multiple times, i.e., employing oversampling. In [10] and [11], it was demonstrated that oversampling can increase the capacity of communication systems with 1-bit quantization to more than 1 bpcu per real dimension. In [12], the results of [10] and [11] were extended to a more realistic system model with intersymbol interference (ISI) which is even beneficial for transmitting with higher-order constellations, especially at high signal-to-noise ratios (SNRs). In [13], the achievable rate for different modulation schemes including higher-order modulation was investigated and the benefit of oversampled 1-bit quantization was confirmed. The authors of [14] showed that higher-order constellations can be detected with 1-bit quantizers in a spatially oversampled system in case the number of receive antennas is sufficiently high and the SNR is appropriate. Thus, these previous works motivate the usage of higher-order constellations for 1-bit quantization.

Furthermore, there are also results on multi-bit quantization. In [15], the achievable rate of massive multiple-input multiple-output (MIMO) systems, which correspond to spatial oversampling, with 1- and 2-bit quantization was analyzed. The results show that the use of higher-order constellations is

This article was presented in part at the 2022 IEEE Latin-American Conference on Communications (LATINCOM) [1]. This work was supported by a gift from Qualcomm Technologies, Inc.

Christian Forsch and Wolfgang Gerstacker are with the Institute for Digital Communications, Friedrich-Alexander-Universität Erlangen-Nürnberg, Erlangen, Germany (e-mail: christian.forsch@fau.de; wolfgang.gerstacker@fau.de).

Peter Zillmann, Osama Alrabadi, and Stefan Brueck are with Qualcomm CDMA Technologies, Nürnberg, Germany (e-mail: pzillman@qti.qualcomm.com; osamaa@qti.qualcomm.com; sbrueck@qti.qualcomm.com).

feasible. In [16], it was also demonstrated that the achievable rate can be increased for 2-bit quantization with higher-order constellations such as 64-ary quadrature amplitude modulation (QAM), and it was shown that the performance in terms of achievable rate for 3-bit quantization is very close to the unquantized case.

In addition to the achievable rate analysis of low-resolution quantization with oversampling, which was mainly conducted in the above referenced works, the performance in terms of error rate for higher-order constellations is of interest. In [17], the symbol error rate (SER) for different symbol sources was analyzed for 1-bit quantization with oversampling. The results indicate that 4-ary amplitude-shift keying (ASK) with independent and uniformly distributed symbols results in a high error floor for the utilized detector. In [18], it was shown via numerical evaluation that the SER for quantization with 1-3 bit for higher-order constellations can be reduced by inducing artificial noise in a maximum ratio combining receiver. The performance for PSK-modulated symbols was investigated in [19] for a massive MIMO scenario with 1-bit quantization. According to the presented SER results, the spatial oversampling enables a reliable detection even for higher-order PSK constellations. There are various further works which deal with massive MIMO systems with low-resolution quantization and higher-order constellations, e.g., [20]–[24]. In these works, different detection schemes are developed and their viability is shown via Monte Carlo simulations.

The above referenced works do not provide any exact analytical results on the SER of higher-order QAM or ASK constellations. Some corresponding results were presented in [25] and [26]. Here, the SER for 1-bit quantization with different oversampling factors and a 4-ASK constellation was analyzed, and the optimal maximum-likelihood (ML) detector was developed. However, multi-bit quantization was not studied in [25] and [26].

More recently, low-resolution quantization has been considered particularly for THz communications. In [27], a transmission with zero crossing modulation (ZXM) signals specifically tailored to 1-bit quantization and temporal oversampling at the receiver is studied in the sub-THz band. Finite-state machines are developed for an efficient demodulation of the ZXM transmit signals. Similarly as in our work, a single-antenna transmitter and a receiver with multiple antennas are assumed in a line-of-sight (LoS) scenario. Conventional linear modulation and higher-order constellations are not considered. In [28], a deep learning-assisted THz receiver is designed for a single-input single-output (SISO) transmission with 1-bit quantization, temporal oversampling, and THz device imperfections. An optimum ML detector is derived for quadrature PSK, and the device imperfections are combatted via a twin-phase training strategy and a neural network based demodulator. In [29], a downlink multi-user indoor THz communication system with distance-aware multi-carrier modulation, an array-of-subarrays architecture with hybrid precoding, and low-resolution digital-to-analog converters (DACs) and ADCs is investigated. The achievable rate is analyzed, and it is shown via numerical results that with moderate resolution DACs and ADCs with 3-5 bit almost the same performance as in the infinite resolution

case can be obtained. No specific modulations are considered, and no error rate analysis is conducted.

In this work, based on [1], we extend the results in [25] and [26] by providing a more detailed analysis on the 1-bit quantization case and considering multi-bit quantization. The generalization to arbitrary quantization resolution is also an extension of our previous work [1]. We consider a simplified channel model as well as a more realistic channel model than in our previous work and show that the developed optimal symbol detector performs well also for realistically modeled THz band indoor channels. We compare different quantization resolutions in a fair manner by constraining the total ADC power consumption to remain constant. Such approach was also adopted in some existing works, e.g., [24] and [30], however, not for higher-order constellations. Moreover, we perform a constellation optimization which was also conducted in [4] and [11]. Here, our approach is different since we do not focus on capacity-achieving constellations but construct constellations which achieve a minimum SER for a given constellation size and SNR. Compared to our previous work [1], we investigate not only 4-ASK but also larger constellations. Our contributions can be summarized as follows:

- We derive the optimal ML detector for an arbitrary quantization resolution when performing the detection based on an average of the oversampled observations in a frequency-flat single-path LoS THz channel.
- We compare the performance of the optimal ML detector to two suboptimal detection schemes. From the SER results, it can be observed that there is a noticeable performance degradation of the suboptimal detectors when the constellation size is larger than the number of quantization levels of the ADC.
- Analytical SER results are presented which are favorable in terms of computation time compared to exhaustive Monte Carlo simulations. Hence, SER curves can be obtained for a fine SNR grid revealing some interesting properties when employing low-resolution quantization in conjunction with higher-order constellations. It can be observed that the SER curves are not smooth and exhibit multiple local minima.
- We compare the performance of quantization with 1-3 bit in a fair manner by keeping the total ADC power consumption constant. Thereby, we show that 1-bit quantization outperforms 2- and 3-bit quantization at low SNRs, even for higher-order constellations.
- We show that our proposed optimal detector also performs well in a realistic indoor THz channel with multipath propagation and ISI.
- We optimize the transmit symbol constellation for 1-bit quantization with respect to the SER. Here, we gain some interesting insights into optimizing higher-order constellations. In particular, the minimum achievable SER can be decreased by increasing the distance of the outermost symbols to the remaining inner symbols of a QAM constellation. The optimization yields very high gains in terms of the minimum achievable SER.

This paper is organized as follows. In Section II, we

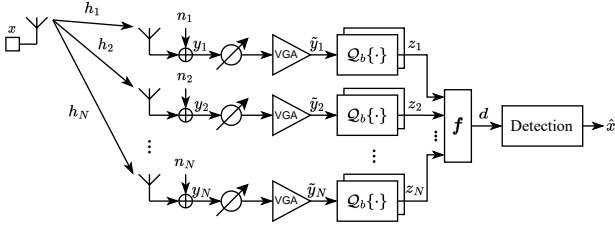


Fig. 1. SIMO LoS THz channel with analog phase shifters, variable gain amplifiers, uniform quantizers, linear filter, and detector at the receiver side.

introduce and motivate the system model. In Section III, the ADC power consumption model is presented, and we specify ADC parametrizations for a prescribed power consumption. In Section IV, we compute the statistics of the considered detection variable and present corresponding detectors, including the optimal ML detector. In Section V, we present numerical results for the SER of the presented detectors. In Section VI, we optimize the transmit constellation with respect to the SER of 1-bit quantization. Some conclusions are drawn in Section VII.

Notation: a , \mathbf{a} , and \mathbf{A} represent a scalar, a column vector, and a matrix, respectively. a_i is the i^{th} element of the vector \mathbf{a} . $(\cdot)^*$ and $(\cdot)^T$ denote the complex conjugate and the transposition operation, respectively. $\text{diag}\{\cdot\}$ is a diagonal matrix with the elements in brackets on the main diagonal. The Hadamard product is given by \odot . $|\mathcal{A}|$ stands for the cardinality of the set \mathcal{A} . $E\{\cdot\}$ is the expectation operator and $\lfloor \cdot \rfloor$ represents the floor function. The set of natural numbers including zero and the set of real numbers are denoted by \mathbb{N}_0 and \mathbb{R} , respectively. $\mathbf{0}_N$, $\mathbf{1}_N$, and \mathbf{I}_N represent an all-zero column vector of length N , an all-ones column vector of length N , and an $N \times N$ identity matrix, respectively. $\mathcal{R}\{\cdot\}$ and $\mathcal{I}\{\cdot\}$ return the real and imaginary part of the argument, respectively. $\mathcal{N}(\boldsymbol{\mu}, \boldsymbol{\Sigma})$ and $\mathcal{CN}(\boldsymbol{\mu}, \boldsymbol{\Sigma})$ denote a real and complex multivariate Gaussian distribution with mean vector $\boldsymbol{\mu}$ and covariance matrix $\boldsymbol{\Sigma}$, respectively. $Q(x) = \frac{1}{\sqrt{2\pi}} \int_x^\infty e^{-\frac{t^2}{2}} dt$ is the Q-function.

II. SYSTEM MODEL

We consider a LoS THz channel with uniform quantization and oversampling at the receiver side. Oversampling is applied in the spatial domain, i.e., we consider a single-input multiple-output (SIMO) system with multiple receive antennas. The corresponding system model is illustrated in Fig. 1. Here, the input symbol $x^c \in \mathcal{X}$ is chosen from a complex finite alphabet \mathcal{X} with cardinality $|\mathcal{X}| = M$ and power $\sigma_x^2 = E_{x^c}\{|x^c|^2\}$.¹ More specifically, an M -ary square QAM constellation with equiprobable symbols is considered. For the following developments, we assume a frequency-flat single-path LoS THz channel which is a valid assumption since non-line-of-sight (NLoS) paths are heavily attenuated due to the use of directional antennas and the additional reflection and scattering loss in the THz band [31]. Furthermore, we consider transmission windows which are

¹We use the superscript $(\cdot)^c$ to denote complex-valued variables. When dealing with real-valued quadrature components later on, we omit this superscript for better readability.

not heavily affected by molecular absorption which renders them practically frequency flat. However, these assumptions are discarded in Subsection V-B where we study a realistic indoor THz channel, modeled based on ray tracing. The SIMO channel with N receive antennas can be described as a vector $\mathbf{h}^c = [h_1^c \dots h_N^c]^T$ with channel coefficients [32]

$$h_i^c = \frac{c}{4\pi f d_i} \cdot e^{-\frac{1}{2}\kappa(f)d_i} \cdot e^{-j2\pi f \frac{d_i}{c}}, \quad (1)$$

where c is the speed of light, f is the operating frequency, d_i denotes the distance between transmitter and receive antenna i , and $\kappa(f)$ stands for the frequency-dependent molecular absorption coefficient. Thus, the first term in (1) accounts for the spreading loss, the second term stands for the molecular absorption loss, and the last term indicates the phase shift the wave experiences when traveling over a distance d_i . At the receiver, the signal is corrupted by additive white Gaussian noise (AWGN) which yields the receive vector

$$\mathbf{y}^c = \mathbf{h}^c x^c + \mathbf{n}^c, \quad (2)$$

with $\mathbf{n}^c \sim \mathcal{CN}(\mathbf{0}_N, \sigma_n^2 \mathbf{I}_N)$. We define the SNR as the ratio of the average received symbol power and the noise power, $\text{SNR} = \frac{\|\mathbf{h}^c\|_2^2 \sigma_x^2}{N \sigma_n^2}$. Before quantization, the noisy receive samples y_i^c are fed into analog phase shifters and variable gain amplifiers (VGAs) which compensate for the channel's phase shift and attenuation. For this, perfect knowledge of the channel coefficients h_i^c is assumed at the receiver. The analog signal processing yields the vector

$$\tilde{\mathbf{y}}^c = \tilde{\mathbf{h}}^{c*} \odot \mathbf{y}^c = x^c \mathbf{1}_N + \tilde{\mathbf{n}}^c, \quad (3)$$

with $\tilde{\mathbf{h}}^c = \left[\frac{h_1^c}{|h_1^c|^2} \dots \frac{h_N^c}{|h_N^c|^2} \right]^T$ and $\tilde{\mathbf{n}}^c \sim \mathcal{CN}(\mathbf{0}_N, \text{diag}\{\frac{\sigma_n^2}{|h_1^c|^2}, \dots, \frac{\sigma_n^2}{|h_N^c|^2}\})$. For co-located receive antennas, the different path gains are approximately the same, i.e., $|h_1^c|^2 \approx \dots \approx |h_N^c|^2 =: |h^c|^2$. Hence, the noise in different branches is independent and identically distributed (i.i.d.), $\tilde{\mathbf{n}}^c \sim \mathcal{CN}(\mathbf{0}_N, \tilde{\sigma}_n^2 \mathbf{I}_N)$ with $\tilde{\sigma}_n^2 = \frac{\sigma_n^2}{|h^c|^2}$. This yields N independent AWGN channels with the same noise variance. Then, the vector $\tilde{\mathbf{y}}^c$ is quantized element-wise by a b -bit quantizer with law $\mathcal{Q}_b^c\{\tilde{y}_i^c\} = \mathcal{Q}_b\{\mathcal{R}\{\tilde{y}_i^c\}\} + j\mathcal{Q}_b\{\mathcal{I}\{\tilde{y}_i^c\}\}$, i.e., real and imaginary part are quantized separately. The quantizer is chosen as a uniform midrise quantization law with step size Δ ,

$$\mathcal{Q}_b\{\tilde{y}_i\} = \begin{cases} \text{sign}(\tilde{y}_i) \cdot \left(\left\lfloor \frac{|\tilde{y}_i|}{\Delta} \right\rfloor \Delta + \frac{\Delta}{2} \right) & \text{for } |\tilde{y}_i| < 2^{b-1} \Delta \\ \text{sign}(\tilde{y}_i) \cdot \frac{(2^b-1)\Delta}{2} & \text{otherwise} \end{cases}, \quad (4)$$

as illustrated in Fig. 2. The resulting vector \mathbf{z}^c is processed by a linear filter $\mathbf{f}^c \in \mathbb{R}^N$ which returns the detection variable

$$d^c = \mathbf{f}^{cT} \mathbf{z}^c = \mathbf{f}^{cT} \mathcal{Q}_b^c\{\tilde{\mathbf{y}}^c\} = \mathbf{f}^{cT} \mathcal{Q}_b^c\{x^c \mathbf{1}_N + \tilde{\mathbf{n}}^c\}. \quad (5)$$

We aim at analyzing the performance of the system for a specific detection filter $\mathbf{f}^c = \frac{1}{N} \mathbf{1}_N$, constituting a simple averaging filter. Finally, the detector returns the estimated input symbol \hat{x}^c .

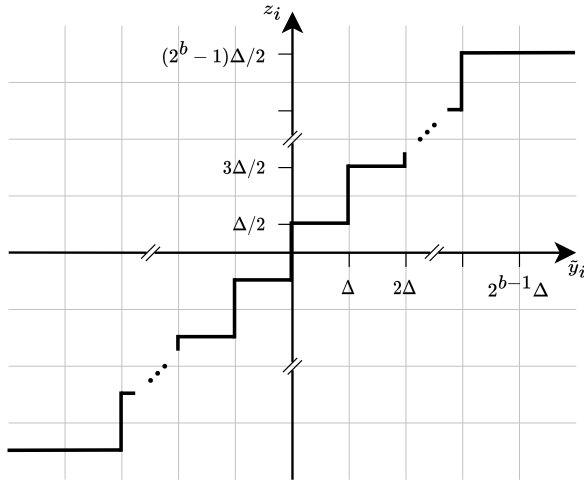


Fig. 2. Law $\mathcal{Q}_b\{\cdot\}$ of b -bit uniform midrise quantizer with step size Δ .

Note that the spatial-wideband effect [33] is not relevant in our scenario since the sampling time of each ADC can be adjusted according to the path delay of the respective antenna. Estimating these delays as well as the channel coefficients in (1) based on quantized observations is beyond the scope of this paper. However, there exist already approaches for such estimation in millimeter-wave channels under low-resolution quantization, cf. e.g., [34]–[37], based on compressive sensing techniques, the expectation-maximization (EM) algorithm, deep generative networks, and a combined ML and least-squares approach, respectively. It is expected that corresponding channel estimation approaches can be also designed for the THz channels considered in this work.

Furthermore, our system model is also applicable to hybrid receivers which are often discussed in the literature. Here, the signal after analog combining in a receiver subarray via phase shifters and an adder would be fed into the VGA before quantization. It should be noted that especially in the case of higher-order modulation, the availability of a sufficient number of quantized observations is crucial, i.e., analog combining should provide a sufficient number of output streams. Finally, we note that VGAs are not necessary in the case of 1-bit quantization. However, the knowledge of the channel gains is still important here for detection.

III. ADC POWER CONSUMPTION

In this section, we introduce the adopted model for the power P_{ADC} consumed in the ADC based on the models in [38]–[41] which can be unified as

$$P_{\text{ADC}} = \gamma \cdot N \cdot 2^{\zeta q} \cdot f_s^\nu, \quad (6)$$

where γ denotes a constant which depends on the utilized ADC technology. Here, one common choice for γ is the Walden figure of merit [42]. Furthermore, N stands for the oversampling factor as introduced in the previous section, q denotes either the total number of bits b used in quantization or the effective number of bits (ENOB) of a given ADC, the parameter $\zeta \in \{1, 2\}$ depends on the quantization resolution,

f_s is the sampling frequency, and the parameter $\nu \in \{1, 2\}$ is related to the sampling frequency. For lower-resolution ADCs, $\zeta = 1$ is usually chosen, whereas $\zeta = 2$ is used for moderate-to-higher-resolution ADCs, and $\nu = 1$ is utilized for small sampling frequencies while $\nu = 2$ for larger sampling frequencies. According to [3] and [43], a doubling of the power consumption when increasing the quantization resolution by 1, i.e., $\zeta = 1$, occurs for ADCs with a signal-to-noise-and-distortion ratio (SNDR) of $\text{SNDR} < 50$ dB which is equivalent to $\text{ENOB} < 8$ bit. Larger sampling frequencies, i.e., $\nu = 2$, correspond to the range $f_s > 100$ MHz [3], [43].

In this work, we analyze the performance of low-resolution ADCs which are primarily of interest for very high sampling frequencies. Hence, we consider the parametrization $\zeta = 1$ and $\nu = 2$. Furthermore, we use $q = b$ which facilitates the power consumption computation of the b -bit quantizer introduced in the last section.² As a consequence of this parametrization, increasing the quantization resolution by 1 bit has the same effect as doubling the oversampling factor N . Therefore, for example, 1-bit quantization ($b = 1$) with an oversampling factor of $N = 64$ results in the same power consumption as using a 2-bit ADC with $N = 32$ or a 3-bit ADC with $N = 16$, respectively. These three cases will be analyzed in Section V in more detail. It should be noted that the linear scaling of the power consumption with respect to the oversampling factor does not contradict the quadratic increase with respect to the sampling frequency f_s according to (6) with $\nu = 2$. Here, the linear scaling with respect to N can be motivated by time-interleaved ADC architectures or by spatial oversampling.

IV. OPTIMAL SYMBOL DETECTION

The optimal ML detector maximizes the probability mass function (PMF) of the detection variable d^c given the input symbol x^c , i.e., $p_{d^c|x^c}(d^c|x^c)$. The resulting ML estimate of the transmitted symbol is

$$\hat{x}^c = \arg \max_{x^c \in \mathcal{X}} p_{d^c|x^c}(d^c|x^c). \quad (7)$$

In order to derive the likelihood function $p_{d^c|x^c}(d^c|x^c)$, the conditional probability distributions of the unquantized and quantized received signals have to be determined first. For this, we make the assumption of co-located receive antennas which yields approximately i.i.d. noise samples. Furthermore, we consider the real and the imaginary part separately which is justified since both components are independent and have the same noise variance according to (3). In the following, we express the fact that we consider only one quadrature component by omitting the superscript $(\cdot)^c$, e.g., x and d denote either the in-phase or the quadrature component of the input symbol x^c and the detection variable d^c , respectively. The ML estimate of the respective quadrature components is, hence, given by

$$\hat{x} = \arg \max_{x \in \mathcal{X}'} p_{d|x}(d|x), \quad (8)$$

²ENOB depends on the actual hardware realization of the ADC. Since we do not consider any specific ADC realization, we use $q = b$.

with the M' -ary quadrature component constellation $\mathcal{X}' = \mathcal{R}\{\mathcal{X}\} = \mathcal{I}\{\mathcal{X}\}$ of the original M -ary square QAM constellation \mathcal{X} where $M' := \sqrt{M}$.

A. Probability Distributions of Received Signals and Detection Variable

For a fixed input symbol x , the unquantized vector $\tilde{\mathbf{y}}$ follows the same probability distribution as the noise vector except for a shift of the mean by x , i.e., $\tilde{\mathbf{y}} \sim \mathcal{N}(x\mathbf{1}_N, \frac{\tilde{\sigma}_n^2}{2}\mathbf{I}_N)$ which implies that the unquantized samples are i.i.d. Gaussian distributed with mean x and variance $\frac{\tilde{\sigma}_n^2}{2}$. We denote the random variable corresponding to one received sample \tilde{y}_n as \tilde{y} . Due to the independent unquantized observations and the element-wise quantization, the quantized vector \mathbf{z} also consists of independent entries if conditioned on x . Therefore, the corresponding likelihood function can be written as

$$p_{\mathbf{z}|x}(\mathbf{z}|x) = \prod_{n=1}^N p_{z|x}(z_n|x), \quad (9)$$

where $p_{z|x}(z_n|x)$ is the PMF of the n^{th} entry of \mathbf{z} given x , $n \in \{1, \dots, N\}$. Here, the quantized samples z_n are realizations of the discrete random variable z which follows a multinoulli distribution with $K = 2^b$ different values $z(k) := (k - \frac{K+1}{2})\Delta$, $k \in \{1, \dots, K\}$. Due to the normally distributed elements in the unquantized vector, the conditional probabilities of the possible values of the random variable z can be computed as

$$\begin{aligned} P_k(x) &:= p_{z|x}(z(k)|x) = p_{y|x}(y \in \mathcal{D}_y(z(k))|x) \\ &= Q\left(\frac{\tau_{\text{low}}(z(k)) - x}{\tilde{\sigma}_n/\sqrt{2}}\right) - Q\left(\frac{\tau_{\text{up}}(z(k)) - x}{\tilde{\sigma}_n/\sqrt{2}}\right), \end{aligned} \quad (10)$$

where the quantizer decision region and corresponding thresholds are given by

$$\mathcal{D}_y(z(k)) = \{y \in \mathbb{R} \mid \tau_{\text{low}}(z(k)) \leq y < \tau_{\text{up}}(z(k))\}, \quad (11)$$

$$\tau_{\text{low}}(z(k)) = \begin{cases} z(k) - \frac{\Delta}{2} & \text{for } z(k) > -\frac{(K-1)\Delta}{2} \\ -\infty & \text{otherwise} \end{cases}, \quad (12)$$

and

$$\tau_{\text{up}}(z(k)) = \begin{cases} z(k) + \frac{\Delta}{2} & \text{for } z(k) < \frac{(K-1)\Delta}{2} \\ +\infty & \text{otherwise} \end{cases}. \quad (13)$$

Now, the mean and the variance of z given x can be calculated as

$$\begin{aligned} \mu_z(x) &= E_{z|x}\{z|x\} \\ &= \Delta \cdot \left(\sum_{k=1}^{K-1} Q\left(\frac{\tau_{\text{up}}(z(k)) - x}{\tilde{\sigma}_n/\sqrt{2}}\right) - \frac{K-1}{2} \right), \end{aligned} \quad (14)$$

$$\begin{aligned} \sigma_z^2(x) &= E_{z|x}\{(z - \mu_z(x))^2|x\} \\ &= \Delta^2 \cdot \left(\sum_{k=1}^{K-1} (2k - K) \cdot Q\left(\frac{\tau_{\text{up}}(z(k)) - x}{\tilde{\sigma}_n/\sqrt{2}}\right) \right. \\ &\quad \left. + \left(\frac{K-1}{2}\right)^2 \right) - \mu_z^2(x), \end{aligned} \quad (15)$$

where we have used the fact that $\tau_{\text{low}}(z(k+1)) = \tau_{\text{up}}(z(k))$ for $k \in \{1, \dots, K-1\}$.

As mentioned above, the random variable z follows a multinoulli distribution with K possible values and is observed N times. We denote the number of observations of the k^{th} value $z(k)$ as $\kappa_k \in \{0, \dots, N\}$ with $\sum_{k=1}^K \kappa_k = N$. Hence, the collection of the numbers of observations is multinomially distributed,

$$p_{\kappa|x}(\kappa|x) = \binom{N}{\kappa_1, \dots, \kappa_K} \prod_{k=1}^K P_k^{\kappa_k}(x), \quad (16)$$

with the vector of numbers of observations $\kappa = [\kappa_1 \dots \kappa_K]$ and the multinomial coefficient $\binom{N}{\kappa_1, \dots, \kappa_K} = \frac{N!}{\kappa_1! \dots \kappa_K!}$. Since the detection variable d is the average of all N observations, it can be expressed in terms of the numbers of observations κ_k ,

$$d = d(\kappa) = \frac{1}{N} \sum_{k=1}^K \kappa_k z(k) = \frac{1}{N} \sum_{k=1}^K \kappa_k \left(k - \frac{K+1}{2} \right) \Delta. \quad (17)$$

Equation (17) can be rearranged as

$$\sum_{k=1}^K \kappa_k k = N \left(\frac{d}{\Delta} + \frac{K+1}{2} \right). \quad (18)$$

Therefore, all vectors κ which satisfy (18) for fixed d yield the same value d of the detection variable. Hence, the PMF of the detection variable is given by a sum of multinomial distributions,

$$p_{d|x}(d = d(\kappa)|x) = \sum_{\kappa \in \mathcal{K}_d} \binom{N}{\kappa_1, \dots, \kappa_K} \prod_{k=1}^K P_k^{\kappa_k}(x), \quad (19)$$

with the set of vectors of numbers of observations corresponding to detection variable value d ,

$$\mathcal{K}_d = \left\{ \kappa \in \mathbb{N}_0^K \mid \sum_{k=1}^K \kappa_k = N \wedge \sum_{k=1}^K \kappa_k k = N \left(\frac{d}{\Delta} + \frac{K+1}{2} \right) \right\}. \quad (20)$$

Note that the detection variable can only take on discrete values from $z(k=1)$ to $z(k=K)$ with a spacing of $\frac{\Delta}{N}$, resulting in $N(K-1) + 1$ possible different values. The set of all possible vectors of numbers of observations $\mathcal{K} = \{\kappa \in \mathbb{N}_0^K \mid \sum_{k=1}^K \kappa_k = N\}$ consists of $|\mathcal{K}| = \binom{N+K-1}{K-1}$ different elements [44]. If $b > 1$ and $N > 1$, there are more elements in \mathcal{K} than possible detection variable values. Hence, there is no one-to-one mapping between κ and d for multi-bit quantization under oversampling which is exemplified in Table I for $b = 2$ and $N = 2$. This means that the receiver is not able to unambiguously determine the vector of numbers of observations κ when inspecting the detection variable d , contrary to 1-bit quantization where always a one-to-one mapping between κ and d exists. This has an influence on the complexity and the performance of the ML detector based

TABLE I
ALL POSSIBLE VECTORS OF NUMBERS OF OBSERVATIONS AND
CORRESPONDING DETECTION VARIABLE VALUES FOR $b = 2$ AND $N = 2$.

κ_1	κ_2	κ_3	κ_4	d
2	0	0	0	$-3/2 \Delta$
1	1	0	0	$-\Delta$
0	2	0	0	$-1/2 \Delta$
1	0	1	0	$-1/2 \Delta$
1	0	0	1	0
0	1	1	0	0
0	1	0	1	$1/2 \Delta$
0	0	2	0	$1/2 \Delta$
0	0	1	1	Δ
0	0	0	2	$3/2 \Delta$

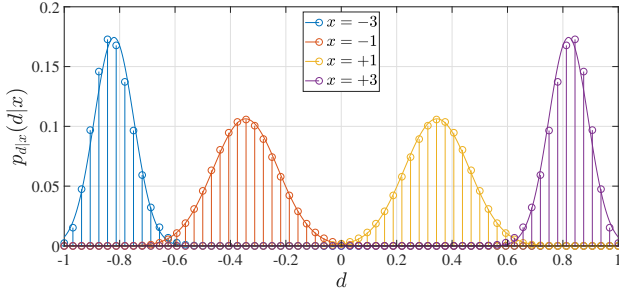


Fig. 3. PMF $p_{d|x}(d|x)$ (19) and (scaled) continuous approximation $f_{d|x,CLT}(d|x)$ (23) for $b = 1$, $\Delta = 2$, $N = 64$, and $\mathcal{X}' = \{\pm 1, \pm 3\}$ at SNR = 0 dB.

on d which will be discussed later on in more detail. The mean and the variance of d can be computed using (14) and (15),

$$\mu_d(x) = E_{d|x}\{d|x\} = \frac{1}{N} \sum_{n=1}^N \mu_z(x) = \mu_z(x), \quad (21)$$

$$\sigma_d^2(x) = E_{d|x}\{(d - \mu_d(x))^2|x\} = \frac{1}{N^2} \sum_{n=1}^N \sigma_z^2(x) = \frac{1}{N} \sigma_z^2(x). \quad (22)$$

Thus, a higher oversampling factor leads to a smaller variance of the detection variable. With the above calculated mean and variance, via the central limit theorem (CLT), we can approximate the PMF of d for large N with a continuous Gaussian probability density function (PDF), $d \sim \mathcal{N}(\mu_d(x), \sigma_d^2(x))$,

$$f_{d|x,CLT}(d|x) = \frac{1}{\sqrt{2\pi}\sigma_d(x)} e^{-\frac{(d - \mu_d(x))^2}{2\sigma_d^2(x)}}. \quad (23)$$

In Fig. 3, the PMF of d as well as the continuous CLT approximation which is scaled with $\frac{\Delta}{N}$ are illustrated for $b = 1$, $\Delta = 2$, $N = 64$, and a 4-ASK constellation, corresponding to 16-QAM when considering both quadrature components. It can be seen that the approximation and the true distribution match very well for the given oversampling factor, input constellation, and SNR. However, there are some limitations to the continuous approximation of the discrete system which will be pointed out later. Furthermore, the variance of d for input symbols with different magnitudes is not equal, resulting in consequences for the ML detector which will be discussed in the next subsection. In Fig. 4, the PMF of d is shown for $b = 3$, $\Delta = 1$, $N = 16$, and otherwise the same parameters

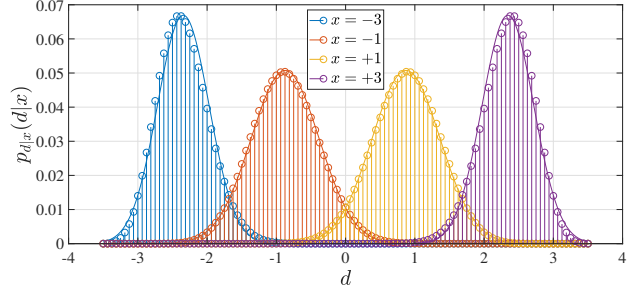


Fig. 4. PMF $p_{d|x}(d|x)$ (19) and (scaled) continuous approximation $f_{d|x,CLT}(d|x)$ (23) for $b = 3$, $\Delta = 1$, $N = 16$, and $\mathcal{X}' = \{\pm 1, \pm 3\}$ at SNR = 0 dB.

as in Fig. 3. Here, the variance of d for different input symbols varies as well. However, the relative difference in the variances is smaller than for 1-bit quantization which makes 3-bit quantization with $N = 16$ closer to the unquantized case where the variances are equal for all input symbols.

B. Symbol Detectors

We can use the PMF in (19) to specify the ML detector according to (8),

$$\hat{x}_{ML} = \arg \max_{x \in \mathcal{X}'} \sum_{\kappa \in \mathcal{K}_d} \binom{N}{\kappa_1, \dots, \kappa_K} \prod_{k=1}^K P_k^{\kappa_k}(x). \quad (24)$$

The complexity of the detector according to (24) is quite high due to the summation of $|\mathcal{K}_d|$ terms, each comprising a multinomial coefficient and a product of K powers. However, for 1-bit quantization, the detector simplifies significantly because $|\mathcal{K}_d| = 1 \forall d$ due to the one-to-one mapping between κ and d , and, therefore, the multinomial coefficient is irrelevant for the maximization with respect to x . Hence, only the product of $K = 2$ powers needs to be computed which was already indicated in [1] and [26]. Moreover, we consider an alternative detector based on the CLT approximation which is given by

$$\hat{x}_{CLT} = \arg \max_{x \in \mathcal{X}'} \frac{1}{\sigma_d(x)} e^{-\frac{(d - \mu_d(x))^2}{2\sigma_d^2(x)}}. \quad (25)$$

In our case, we cannot employ the classical ML approach for an unquantized channel and minimize the Euclidean distance between d and $\mu_d(x)$ in order to realize (25) because the variance $\sigma_d^2(x)$ depends on x . Therefore, in general, the optimal decision thresholds do not lie exactly in the middle between the mean values $\mu_d(x)$ of adjacent input symbols. Nevertheless, we investigate the performance of such suboptimal approach as well with decision rule

$$\hat{x}_{minDist} = \arg \min_{x \in \mathcal{X}'} (d - \mu_d(x))^2. \quad (26)$$

The three detectors according to (24), (25), and (26) result in three different sets of decision thresholds. In Fig. 5, the thresholds between decision regions for $x = +1$ and $x = +3$ are depicted exemplarily for 1-bit quantization.

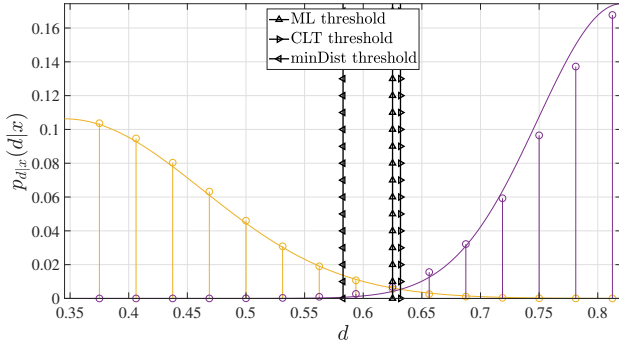


Fig. 5. Thresholds between the decision regions for $x = +1$ and $x = +3$ according to the detectors (24), (25), and (26) for $b = 1$, $\Delta = 2$, $N = 64$, and $\mathcal{X}' = \{\pm 1, \pm 3\}$ at SNR = 0 dB. The colored discrete markers and continuous lines represent the PMF $p_{d|x}(d|x)$ (19) and (scaled) continuous approximation $f_{d|x,CLT}(d|x)$ (23), respectively.

The fully optimum ML detector is directly based on the quantized vector \mathbf{z} , i.e., no filter \mathbf{f}^c is applied, and can be expressed via the likelihood function in (9), resulting in

$$\hat{x}_{\text{noFilt}} = \arg \max_{x \in \mathcal{X}'} p_{\mathbf{z}|x}(\mathbf{z}|x) = \arg \max_{x \in \mathcal{X}'} \prod_{k=1}^K P_k^{\kappa_k}(x). \quad (27)$$

According to (27), the exact vector \mathbf{z} is not relevant for detection but the numbers of observations κ_k , $k \in \{1, \dots, K\}$, are a set of sufficient statistics which was also mentioned in [9] for 1-bit quantization. Due to the one-to-one mapping between d and κ in case of 1-bit quantization, which makes the averaging filtering an invertible operation, it can be easily shown via the data processing theorem [45] that the detector in (24) is equivalent to the fully optimum detector in (27). As a consequence, the averaging filter \mathbf{f}^c is optimal for the considered system with $b = 1$. For $b > 1$ and $N > 1$, however, this is not the case anymore due to the many-to-one mapping between the numbers of observations and the detection variable, exemplified in Table I. Therefore, for multi-bit quantization with oversampling, the detector in (24) performs worse than the optimal detector in (27). However, the performance loss is negligible as will be observed later from the numerical results.

C. Symbol Error Rate Computation

In order to compute the SER analytically for a given detector, $M' - 1$ decision boundaries $[b_1 \ b_2 \ \dots \ b_{M'-1}]$ per quadrature component have to be determined first. Without loss of generality, an ordering of the constellation symbols $x_i \in \mathcal{X}'$ is assumed, i.e., $x_1 < x_2 < \dots < x_{M'}$. For the ML detector in (24) and the CLT-based detector in (25), the decision threshold b_i can be found by comparing the PMF (19) and PDF (23), respectively, for the two adjacent input symbols x_i and x_{i+1} , and choosing the smallest argument value of d where the function value corresponding to the greater symbol x_{i+1} is higher than or equal to the function value corresponding to the smaller symbol x_i . For the suboptimal detector (26), the i^{th} decision threshold is given by $b_i = \frac{\mu_d(x_i) + \mu_d(x_{i+1})}{2}$ with $\mu_d(x)$ from (21). In general, the decision boundaries depend

on the noise variance and, therefore, have to be recalculated in case the SNR changes.

For computing the SER analytically via the detection variable d , we define for each possible quadrature input symbol x_i a decision region \mathcal{D}_i for the detection variable which depends on the utilized detector. Given the transmitted symbol is x_1 , a detection error occurs if the detection variable d is equal to or above the boundary b_1 . Thus, the decision region for x_1 is $\mathcal{D}_1 = [z(k=1), b_1)$. For the last symbol $x_{M'}$, a wrong symbol will be detected if d is smaller than $b_{M'-1}$, thus $\mathcal{D}_{M'} = [b_{M'-1}, z(k=K)]$. The decision region for any inner symbol x_i , $i \in \{2, \dots, M' - 1\}$, is given by $\mathcal{D}_i = [b_{i-1}, b_i)$. Correspondingly, the SER of one quadrature component for all detectors based on d can be expressed as

$$\text{SER}_{\text{ASK}} = \frac{1}{M'} \sum_{x_i \in \mathcal{X}'} \sum_{d \notin \mathcal{D}_i} p_{d|x}(d|x_i), \quad (28)$$

using the likelihood function $p_{d|x}(d|x)$ in (19).

In order to compute the SER analytically for the detector utilizing \mathbf{z} , we can evaluate the likelihood function in (9) for all possible quantized vectors \mathbf{z} and all possible input symbols x and then find suitable decision sets for all x . However, there are K^N possible quantized vectors which might be too many for an efficient SER computation. Instead, we can compute the conditional probabilities of all possible vectors of numbers of observations $\kappa \in \mathcal{K}$ for each input symbol x , $p_{\kappa|x}(\kappa|x)$, according to (16). Then, we find the most probable symbol x_i for each vector κ based on the computed probabilities and include the considered vector κ in the decision set of the corresponding symbol x_i , $\mathcal{K}_i = \{\kappa \in \mathcal{K} | p_{\kappa|x}(\kappa|x_i) \geq p_{\kappa|x}(\kappa|x_j) \ \forall j \neq i\}$, where we do not allow a vector κ to belong to multiple decision sets. The resulting SER of one quadrature component is given by

$$\text{SER}_{\text{ASK,noFilt}} = \frac{1}{M'} \sum_{x_i \in \mathcal{X}'} \sum_{\kappa \notin \mathcal{K}_i} p_{\kappa|x}(\kappa|x_i). \quad (29)$$

Due to the orthogonality of in-phase and quadrature components, the SER of the complex-valued input symbols $x \in \mathcal{X}$ is given by

$$\text{SER} = 1 - (1 - \text{SER}')^2 = 2 \cdot \text{SER}' - \text{SER}'^2, \quad (30)$$

where SER' is the SER of one quadrature component, obtained from (28) or (29).

V. NUMERICAL RESULTS

A. Frequency-Flat Single-Path LoS THz Channel

In the following, SER results for the frequency-flat single-path LoS THz channel with co-located receive antennas, as introduced in Section II, are presented for the derived detectors and the three ADC parametrizations mentioned in Section III. Here, the exact choice of the transmit power, the carrier frequency, the distance between transmitter and receiver, or the noise variance is not important since the performance finally depends on the SNR. Therefore, we do not specify these individual parameters here. The following results are valid for any combination of the aforementioned parameters which yield a given SNR value. A realistic choice of parameters

for THz communications is made in the next subsection. Moreover, we have computed the SER of an unquantized system with the same oversampling factor as ultimate benchmark which is equivalent to a single-antenna receiver with noise variance $\frac{\sigma_n^2}{N}$. In this case, the presented suboptimal decision boundaries become optimal since the variance of the detection variable for different input symbols become equal and minimizing the Euclidean distance is optimal. Besides, we have conducted Monte Carlo simulations with 10^8 random symbol transmissions in each case in order to verify the analytical results. Furthermore, for 2- and 3-bit quantization, the choice of the step size Δ is important. We will not optimize the step size analytically. However, we heuristically choose different step sizes for $b = 2$ and $b = 3$, depending on the transmit symbol constellation. For 16-QAM transmissions with $\mathcal{X}' = \{\pm 1, \pm 3\}$, we choose the step size to be $\Delta = 2$ for $b = 2$ and $\Delta = 1$ for $b = 3$ such that the constellation symbols are evenly spread over the quantization region. For 64-QAM transmissions with $\mathcal{X}' = \{\pm 1, \pm 3, \pm 5, \pm 7\}$, we choose $\Delta = 4$ for $b = 2$ and $\Delta = 2$ for $b = 3$ for the same reason.

At first, we consider a 16-QAM constellation with $\mathcal{X}' = \{\pm 1, \pm 3\}$. The corresponding SER curves are illustrated in Fig. 6. For 1-bit quantization (Fig. 6a), we observe that the SER curves are not smooth. This behavior stems from the strong nonlinearity in the system and the discrete nature of the detection variable and can be only observed when the resolution with respect to the SNR-axis, based on which the curves are drawn, is sufficiently high. Using our analysis, the SER results can be computed very fast for arbitrary SNR values which is not feasible for exhaustive Monte Carlo simulations. Furthermore, it can be observed that the SER degrades for high SNR and converges to 0.75 as expected due to the fact that at high SNR the four symbols in each quadrant, e.g., $1+j$, $1+3j$, $3+j$ and $3+3j$ in the first quadrant, cannot be distinguished anymore since they are all mapped to the same quantization level due to the negligible influence of noise. Furthermore, one can observe from Fig. 6a that the decision rule based on the continuous CLT approximation leads to a significant performance degradation compared to the optimal ML detector. Besides, the other suboptimal approach based on minimizing the Euclidean distance also leads to a significant performance degradation compared to the ML detector. Furthermore, it can be observed that the ML detector based on the detection variable d in (24) shows exactly the same performance as the fully optimum ML detector based on the quantized vector \mathbf{z} in (27) which was already mentioned in Subsection IV-B. Finally, the performance gap between 1-bit quantization and the unquantized case seems acceptable when considering the benefit of possible power savings in a real system. Here, the loss in SNR equals 2.3 dB, 3.2 dB, and 6.0 dB at an error rate of $\text{SER} = 10^{-1}$, $\text{SER} = 10^{-2}$, and $\text{SER} = 10^{-3}$, respectively.

For 2-bit quantization (Fig. 6b), a performance deviation between the optimal ML detector based on d and both suboptimal detectors can be still observed even though the number of quantization levels is equal to the number of possible input symbols. Only for 3-bit quantization (Fig. 6c), there is almost

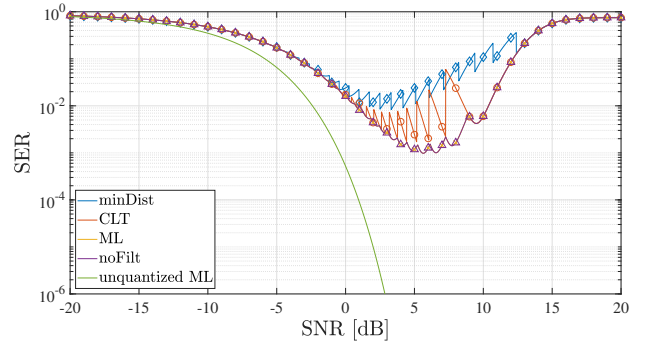
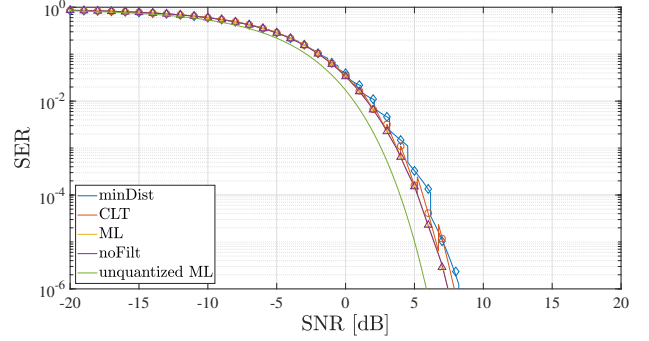
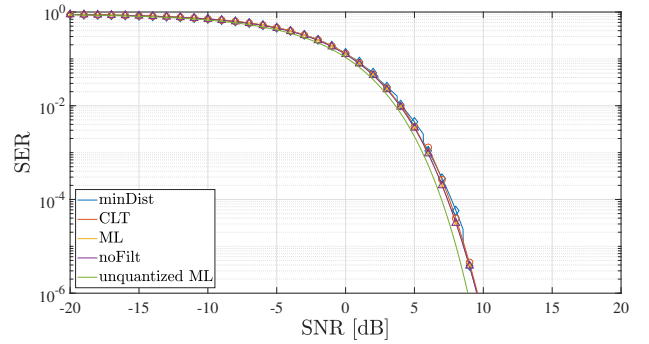
(a) $b = 1$, $N = 64$.(b) $b = 2$, $N = 32$, $\Delta = 2$.(c) $b = 3$, $N = 16$, $\Delta = 1$.

Fig. 6. Analytical SER (solid lines) and simulated SER (markers) for the ML detector (24), CLT-based detector (25), minimum distance detector (26), and fully optimum detector without filtering (27) under 16-QAM transmission with $\mathcal{X}' = \{\pm 1, \pm 3\}$. Furthermore, the ML detection performance for the unquantized case with the same oversampling factor is shown.

no noticeable difference between the three detectors. Zooming in the curves for 2- and 3-bit quantization (not shown here), one observes a small performance loss of the ML detector in (24) compared to the fully optimum detector in (27). This loss is related to the nonexistent one-to-one mapping between the vectors of numbers of observations κ and the detection variable values d which was discussed in Subsection IV-A. However, the loss is negligibly small, thus, the combination of the quantized observations via an averaging filter does practically not degrade the system performance and yields near-optimum results. Besides, it can be noticed for 2- and 3-bit quantization that the SER goes to zero for increasing SNR because the number of quantization levels is larger or equal to the number of possible input symbols. Nevertheless, there is still a performance loss compared to the unquantized case,

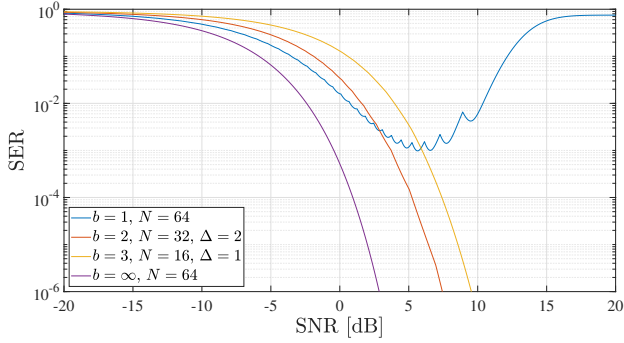


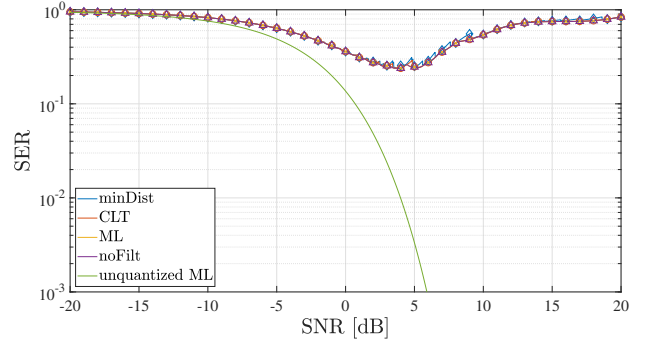
Fig. 7. Analytical SER for the ML detector (24) and different ADC parametrizations under 16-QAM transmission with $\mathcal{X}' = \{\pm 1, \pm 3\}$.

even for 3-bit quantization. Finally, it can be observed that the analytically obtained SER results match exactly with the SER results obtained by Monte Carlo simulations. This confirms that our analysis is accurate. In Fig. 7, the performance of the different ADC parametrizations is compared for the ML detector (24). Here, 1-bit quantization is superior to multi-bit quantization over a relatively large SNR region up to 2.9 dB. For higher SNR, 2-bit quantization always yields the smallest SER. Hence, it seems to be not useful to increase the quantization resolution beyond $\log_2(M')$ bit.

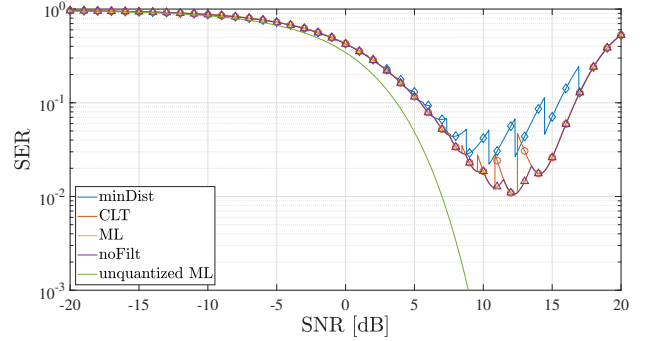
Next, we analyze the SER performance for a 64-QAM constellation with $\mathcal{X}' = \{\pm 1, \pm 3, \pm 5, \pm 7\}$ in Fig. 8. The minimum SER for 1-bit quantization is quite high at approximately 0.24 due to the large constellation and low resolution. Here, the performance could be enhanced by increasing the number of receive antennas N . The receiver with 2-bit quantization yields a minimum SER of $\text{SER} = 10^{-2}$. Besides, the SER increases for $b = 1$ and $b = 2$ at high SNR because there are more constellation symbols than quantization levels. For 3-bit quantization, the SER decays to zero for high SNR as expected. Furthermore, we observe a performance gap between the optimal detector based on d and the two suboptimal detectors as in the 16-QAM transmission case. Moreover, it can be observed again that the analytically obtained SER results match exactly with the SER results obtained by Monte Carlo simulations. Finally, when comparing the results for the different ADC parametrizations in Fig. 9, we deduce that 1-bit quantization performs best up to an SNR of approximately 2.2 dB. Then, there is an SNR window up to approximately 10.8 dB for which 2-bit quantization yields the minimum SER. However, for $\text{SNR} > 10.8$ dB, 3-bit quantization performs best. For both 16-QAM and 64-QAM transmission, at low SNRs below a certain threshold, 1-bit quantization yields the smallest SER when constraining the ADC power consumption to be constant.

B. Realistic Indoor THz Channel

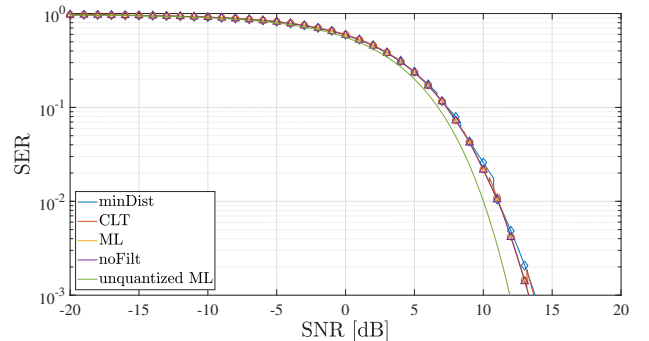
In this subsection, we consider a realistic frequency-selective indoor THz channel with multipath propagation including reflected and scattered rays and adopt a corresponding ray tracing based channel model [46]. We show that our proposed ML detector (24) performs similarly well for this



(a) $b = 1$ and $N = 64$.



(b) $b = 2$, $N = 32$, $\Delta = 4$.



(c) $b = 3$, $N = 16$, $\Delta = 2$.

Fig. 8. Analytical SER (solid lines) and simulated SER (markers) for the ML detector (24), CLT-based detector (25), minimum distance detector (26), and fully optimum detector without filtering (27) under 64-QAM transmission with $\mathcal{X}' = \{\pm 1, \pm 3, \pm 5, \pm 7\}$. Furthermore, the ML detection performance for the unquantized case with the same oversampling factor is shown.

realistic scenario as for the simplified scenario of a frequency-flat single-path LoS channel, analyzed in Subsection V-A. We consider data transmission at a carrier frequency of 300 GHz with a bandwidth of 20 GHz in a large rectangular room with a length, width, and height of 10 m, 20 m, and 2.5 m, respectively. The walls of the room are made of plaster "sample s2" from [47] which has a high roughness. We assume a transmit power of 13 dBm [48] and employ a root-raised-cosine (RRC) filter with a roll-off factor of 0.25 at both transmitter and receiver side. This results in a data rate of 64 Gbps and 96 Gbps for 16- and 64-QAM transmission, respectively. Furthermore, we consider perfectly aligned horn antennas at both the transmitter and the receiver. Here, we use the Gaussian beam model for the radiation pattern of the horn antenna with a gain of 18.9 dBi [49]. Besides, we utilize

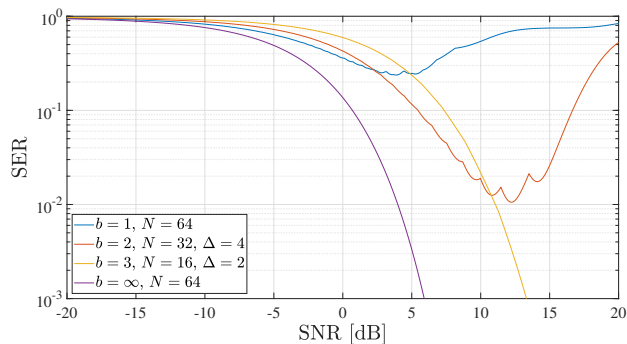


Fig. 9. Analytical SER for the ML detector (24) and different ADC parametrizations under 64-QAM transmission with $\mathcal{X}' = \{\pm 1, \pm 3, \pm 5, \pm 7\}$.

TABLE II
THZ SIMULATION PARAMETERS.

Parameter	Value
Carrier frequency	300 GHz
Bandwidth	20 GHz
Distance	1-17 m
Wall material	Plaster
Transmit power	13 dBm
Transmit pulse and receive filter	RRC filter with roll-off factor 0.25
Transmit and receive antennas	Horn antenna with 18.9 dBi gain
Noise power density	-174 dBm/Hz
Noise figure	15 dB

a uniform planar array (UPA) with $\lambda/2$ antenna spacing at the receiver with 8×8 , 8×4 , and 4×4 antennas in the horizontal and vertical direction for $N = 64$, $N = 32$, and $N = 16$, respectively. Finally, the noise power density is set to -174 dBm/Hz, and a noise figure of 15 dB is selected. The simulation parameters are summarized in Table II.

The transmitter is placed at one side of the room at the coordinates 5 m, 1.5 m, 2.4 m as illustrated in Fig. 10. The receiver is located at a height of 1.5 m at nine different distances from the transmitter, ranging from 1 m to 17 m. For each distance, we consider three different positions of the receiver: one in the middle of the room, one close to the wall, and one in between as can be also observed from Fig. 10. For each receiver position, we transmit 100 independent blocks, each consisting of 10^4 consecutive symbols. ISI occurs only between the symbols within one block due to protection intervals between the blocks. Then, the SER results corresponding to the three different positions with a given distance are averaged. Hence, we consider in total $3 \cdot 10^6$ symbol transmissions for each distance. Finally, in order to guarantee a good detection performance even for small distances, i.e., for high SNR, we add artificial noise in front of the ADCs for 16-QAM and 64-QAM transmission in case of 1-bit quantization and for 64-QAM transmission in case of 2-bit quantization, respectively. The optimum power of the artificial noise is determined by inspecting the analytical results from Subsection V-A and identifying the SNR value which yields the smallest SER. According to Figs. 6a and 8a, this optimum SNR value is given by approximately 5.6 dB and 3.8 dB for 16-QAM and 64-QAM transmission, respectively, in case of 1-bit quantization. For 2-bit quantization and 64-QAM, the

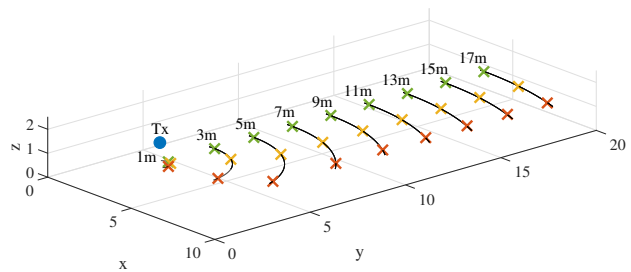


Fig. 10. Indoor environment with transmitter and receiver positions.

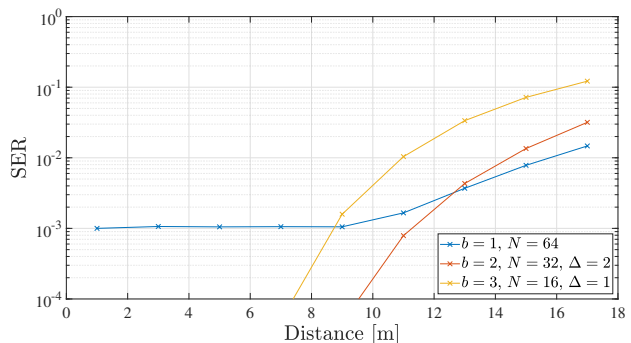


Fig. 11. Simulated SER versus distance in a realistic indoor THz channel for the ML detector (24) and different ADC parametrizations under 16-QAM transmission with $\mathcal{X}' = \{\pm 1, \pm 3\}$.

optimum SNR value is 12.2 dB according to Fig. 8b. Note that these optimum SNR values can be only reached when the actual SNR is larger than the optimum value which is the case for relatively small distances. When the actual SNR is lower than the optimum value, i.e., for large distances, we cannot enhance the performance by adding artificial noise.

In Fig. 11, SER versus the communication distance is shown for 16-QAM. Here, we can observe that 2-bit quantization performs best at small distances. This is in agreement with the results in Fig. 7 for high SNR. For distances larger than 13 m, 1-bit quantization performs best. Furthermore, we observe that adding artificial noise before 1-bit quantization enhances the performance for small distances and keeps the error rate constant up to a distance of approximately 9 m. In this case, the SER is as small for sufficiently small distances as for the simplified frequency-flat single-path LoS channel in Fig. 6a. Hence, we conclude that the simplifying assumptions are justified for the considered indoor THz channel, i.e., ISI can be neglected, and all channel gains are approximately equal. Hence, our proposed detector is still (close-to-)optimal in this case. SER versus distance for 64-QAM transmission is shown in Fig. 12. Here, similar observations can be made as in case of 16QAM before. 1- and 2-bit quantization benefit from adding artificial noise, whereas 3-bit quantization only performs best at small distances. A comparison with the results of Fig. 8 again confirms the validity of the simplifying assumptions adopted for detector design.

It should be noted that a similar performance can be also attained for larger distances by increasing the SNR via, e.g., increasing the transmit power, using more directional antennas, or decreasing the noise level at the receiver.

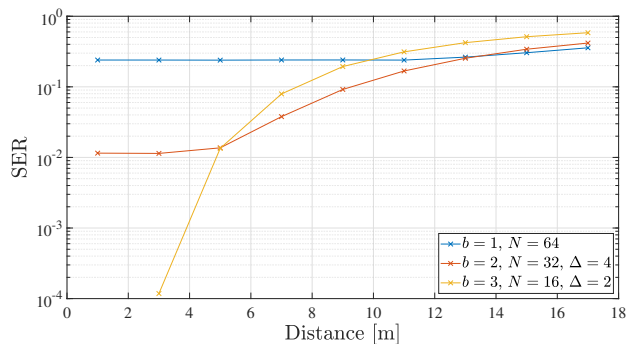


Fig. 12. Simulated SER versus distance in a realistic indoor THz channel for the ML detector (24) and different ADC parametrizations under 64-QAM transmission with $\mathcal{X}' = \{\pm 1, \pm 3, \pm 5, \pm 7\}$.

VI. CONSTELLATION OPTIMIZATION FOR 1-BIT QUANTIZATION

One main difference of the statistics of the detection variable d compared to those of the detection variable $y = x + n$ of an unquantized Nyquist-rate sampling transmission is that the variance of d depends on the transmitted symbol, whereas the variance of y is identical for all input symbols. Due to the equal variance in the unquantized case, it is optimal to place the input symbols equidistantly, i.e., $|x_1 - x_2| = |x_2 - x_3| = \dots = |x_{M'-1} - x_{M'}|$. However, for the quantized system, this is not valid anymore. Especially for 1-bit quantization, the variance can vary significantly for different input symbols as can be seen in Fig. 3. Therefore, it is not obvious what is the optimum constellation which yields a minimum SER. In the following, we aim at determining the optimum constellation for 1-bit quantization. We focus on square 16-, 36-, and 64-QAM constellations with one, two, and three degrees of freedom, respectively, for constellation optimization. Here, the inner four symbols are fixed to $\pm 1 \pm j$, whereas the outer symbols are variable. Therefore, the quadrature component constellations are given by $\mathcal{X}' = \{\pm 1, \pm a_1\}$ for 16-QAM, $\mathcal{X}' = \{\pm 1, \pm a_1, \pm a_2\}$ for 36-QAM, and $\mathcal{X}' = \{\pm 1, \pm a_1, \pm a_2, \pm a_3\}$ for 64-QAM. We find the optimal constellations empirically in each case by comparing SER for different choices of the available free parameters. Similar analyses can be done for 2- and 3-bit quantization. However, here, the choice of the quantizer step size Δ has to be considered as well.

In Fig. 13, analytically obtained SER curves are shown for the ML detector (24) and various 16-QAM constellations with different values of a_1 . It can be observed that the minimum SER can be decreased significantly by increasing a_1 . For example, the minimum SER for $a_1 = 3$ is $9.8 \cdot 10^{-4}$, while the constellation with $a_1 = 8$ yields a minimum SER of $4.5 \cdot 10^{-7}$. This emphasizes the importance of choosing an optimized constellation. However, the minimum SER for $a_1 = 8$ is achieved at a higher SNR than that for $a_1 = 3$. Another interesting observation can be made for $a_1 > 8$. Here, the location of the minimum SER moves to higher SNR for increasing a_1 while the minimum SER value itself does not decrease anymore. This suggests that the minimum SER, illustrated in Fig. 14, converges to a fixed value for increasing a_1 , and $a_1 \approx 8$ is

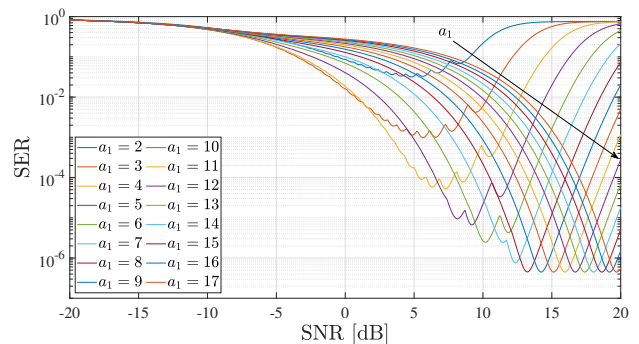


Fig. 13. Analytical SER for the ML detector (24) and different 16-QAM constellations with $\mathcal{X}' = \{\pm 1, \pm a_1\}$, $b = 1$, and $N = 64$.

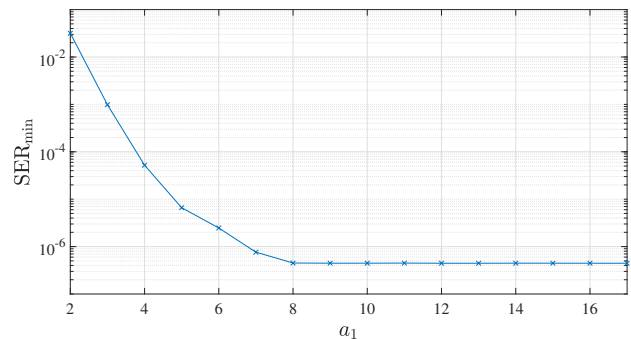


Fig. 14. Minimum SER for the ML detector (24) and different 16-QAM constellations with $\mathcal{X}' = \{\pm 1, \pm a_1\}$, $b = 1$, and $N = 64$.

the smallest outer quadrature component constellation point for which this value can be reached closely. However, the outer constellation point with this property depends on the oversampling factor. Hence, the constellation optimization has to be carried out individually for each oversampling factor of interest. Furthermore, we note that the results indicate that for increasing SNR the optimal outer points will become larger or equivalently the inner points shrink when including a power normalization into the constellation. For $\text{SNR} \rightarrow \infty$, this will result in a 9-QAM constellation which was also proven to be optimal in [11]. Some further results on optimized 16-QAM constellations can be found in [1].

Next, we investigate the SER performance for different 36-QAM constellations, illustrated in Fig. 15. Here, a large number of constellations is considered with integer values for a_1 and a_2 , and $2 \leq a_1 < a_2 \leq 17$. As for the 16-QAM constellations, we observe different minimum SER values for different constellations, while multiple constellations yield the same minimum SER at different SNR. The minimum SER versus the constellation parameters a_1 and a_2 is shown in Fig. 16. Here, also non-integer values of a_1 and a_2 have been included. From the analytically obtained SER values, it can be observed that, similarly to the 16-QAM case, the minimum SER converges for $a_1 = 3.3$ and $a_2 > 11$. Hence, we can conclude that the position of the optimum middle quadrature component constellation point is almost identical to the classical case with $a_1 = 3$, but the position of the outer constellation point is moved to much higher values compared to the standard constellation. Also, we can observe from

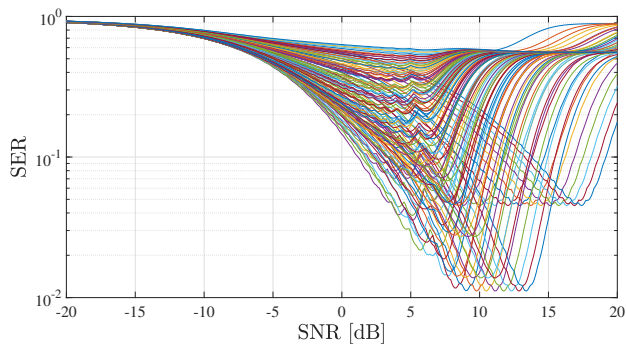


Fig. 15. Analytical SER for the ML detector (24) and different 36-QAM constellations with $\mathcal{X}' = \{\pm 1, \pm a_1, \pm a_2\}$, $b = 1$, and $N = 64$.

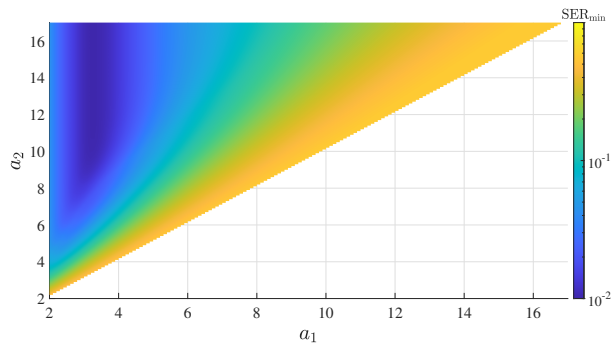


Fig. 16. Minimum SER for the ML detector (24) and different 36-QAM constellations with $\mathcal{X}' = \{\pm 1, \pm a_1, \pm a_2\}$, $b = 1$, and $N = 64$.

Fig. 16 that selecting a large value for a_1 or choosing a_2 close to a_1 always results in a poor performance. For the classical constellation with $a_1 = 3$ and $a_2 = 5$, a minimum SER of $8.4 \cdot 10^{-2}$ is achieved, while for the optimized constellation with $a_1 = 3.3$ and $a_2 > 11$ a SER of approximately $1.0 \cdot 10^{-2}$ cannot be undercut.

Now, we study 64-QAM constellations with three degrees of freedom, a_1 , a_2 , and a_3 . The corresponding SER versus SNR is depicted in Fig. 17 for different constellations with integer constellation points with $2 \leq a_1 < a_2 < a_3 \leq 17$. A similar behavior as for 16- and 36-QAM constellations can be recognized. The same holds for the minimum SER which is illustrated in Fig. 18 for integer values of a_1 , a_2 , and a_3 for simplicity. However, we also conducted a full search over a finer grid, showing that a minimum SER of approximately $1.0 \cdot 10^{-1}$ is achieved for $a_1 = 3.1$, $a_2 = 5.7$, and $a_3 > 14$, whereas the classical constellation yields a minimum SER of $2.4 \cdot 10^{-1}$.

Finally, we motivate the reduction of SER for the optimized constellations. For 16-, 36-, and 64-QAM transmission, we observed that the minimum SER can be decreased by increasing the distance of the outermost constellation points to the remaining inner constellation points and simultaneously keeping the inner points almost equidistantly. This behavior can be explained by comparing the PMFs $p_{d|x}(d|x)$ (19) conditioned on the symbols of the classical constellation and the optimized constellation at the SNR which yields the minimum SER, respectively, shown in Fig. 19. For 16-QAM, the main difference between the two PMFs is that for

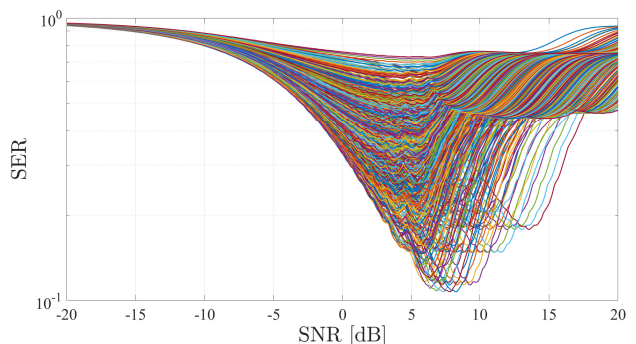


Fig. 17. Analytical SER for the ML detector (24) and different 64-QAM constellations with $\mathcal{X}' = \{\pm 1, \pm a_1, \pm a_2, \pm a_3\}$, $b = 1$, and $N = 64$.

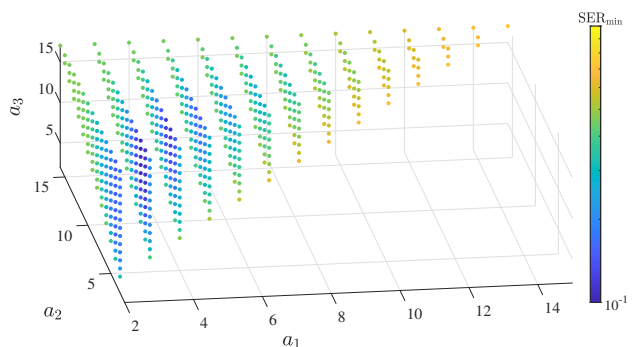


Fig. 18. Minimum SER for the ML detector (24) and different 64-QAM constellations with $\mathcal{X}' = \{\pm 1, \pm a_1, \pm a_2, \pm a_3\}$, $b = 1$, and $N = 64$.

the optimized constellation (Fig. 19b) the probability mass for the outer symbols is concentrated in a single detection variable value $d = \pm 1$, whereas for the classical constellation (Fig. 19a) the probability mass for the outer symbols is spread over essentially three detection variable values. Therefore, the overlap between the probability mass for the outer constellation point and the probability mass for the inner constellation point is smaller for the optimized constellation, and, hence, the SER is reduced. The same holds for 64-QAM transmission, cf. Figs. 19c and 19d. In Table III, the SERs of single quadrature component constellation symbols are collected. It can be observed that for a given classical constellation the error rates of all symbols are of same order of magnitude. However, this is not true anymore for the optimized constellations. Here, the error rate of the outer constellation points is negligible which is in accordance with the previously presented PMFs. Hence, SER is determined by the remaining inner symbols. Also, the reduction in error rate compared to the classical constellation is smaller for the inner symbols than for the outer symbols. This explains why optimizing the constellation yields a higher gain for 16-QAM than for 64-QAM.

VII. CONCLUSION

In this work, we have investigated the SER performance of a THz band transmission with uniform multi-bit quantization and spatial oversampling at the receiver. At first, we considered the ADC power consumption in general and determined different low-resolution reception schemes with equal ADC

TABLE III
ERROR RATES OF SINGLE QUADRATURE COMPONENT CONSTELLATION SYMBOLS $x \in \mathcal{X}'$ AT OPTIMUM SNR FOR THE ML DETECTOR (24) WITH $b = 1$ AND $N = 64$.

Classical constellation								
$x \in \mathcal{X}'$	-7	-5	-3	-1	+1	+3	+5	+7
16-QAM	/	/	$3.9 \cdot 10^{-4}$	$6.0 \cdot 10^{-4}$	$6.0 \cdot 10^{-4}$	$3.9 \cdot 10^{-4}$	/	/
36-QAM	/	$4.6 \cdot 10^{-2}$	$7.1 \cdot 10^{-2}$	$1.3 \cdot 10^{-2}$	$1.1 \cdot 10^{-2}$	$7.1 \cdot 10^{-2}$	$4.6 \cdot 10^{-2}$	/
64-QAM	$1.0 \cdot 10^{-1}$	$2.9 \cdot 10^{-1}$	$9.0 \cdot 10^{-2}$	$3.7 \cdot 10^{-2}$	$2.8 \cdot 10^{-2}$	$9.0 \cdot 10^{-2}$	$2.9 \cdot 10^{-1}$	$1.0 \cdot 10^{-1}$

Optimized constellation								
$x \in \mathcal{X}'$	$-a_3$	$-a_2$	$-a_1$	-1	+1	$+a_1$	$+a_2$	$+a_3$
16-QAM	/	/	$7.6 \cdot 10^{-41}$	$5.6 \cdot 10^{-7}$	$3.3 \cdot 10^{-7}$	$7.6 \cdot 10^{-41}$	/	/
36-QAM	/	$7.6 \cdot 10^{-12}$	$9.2 \cdot 10^{-3}$	$7.4 \cdot 10^{-3}$	$5.1 \cdot 10^{-3}$	$9.2 \cdot 10^{-3}$	$7.6 \cdot 10^{-12}$	/
64-QAM	$2.2 \cdot 10^{-5}$	$7.6 \cdot 10^{-2}$	$7.4 \cdot 10^{-2}$	$7.1 \cdot 10^{-2}$	$5.4 \cdot 10^{-2}$	$7.4 \cdot 10^{-2}$	$7.6 \cdot 10^{-2}$	$2.2 \cdot 10^{-5}$

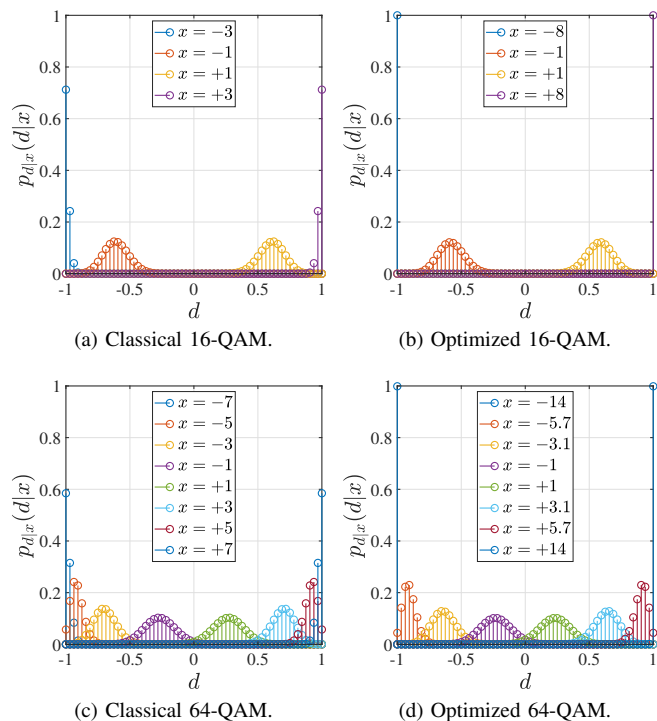


Fig. 19. PMF $p_{d|x}(d|x)$ (19) for $b = 1$, $\Delta = 2$, $N = 64$, and different constellations at optimum SNR, respectively.

power consumption for a fair comparison. Then, the statistics of the detection variable which is generated by combining the quantized observations have been analyzed. We have formulated the ML detector as well as several suboptimal detection schemes. It has been shown that the ML detector for 1-bit quantization has a significantly reduced complexity compared to multi-bit quantization. Furthermore, our results indicate that the suboptimal detection schemes perform noticeably worse than the optimal ML detector when the constellation size is larger than the number of quantization levels of the ADC. We have also shown that 1-bit quantization outperforms 2- and 3-bit quantization at low SNRs even in case of a transmission with more than 1 bpcu per real dimension. Then, we have determined SER-optimized 16-, 36-, and 64-QAM symbol constellations for 1-bit quantization. Here, the minimum SER can be decreased significantly by increasing the distance of

the outermost symbols to the remaining inner symbols. The effect of this outer point movement is especially strong for small constellations, resulting in a SER reduction by several orders of magnitude.

In future work, we want to generalize our findings on optimum constellations to multi-bit quantization and arbitrary oversampling factors and constellation sizes. Furthermore, channel estimation with low-resolution ADCs and the consequences of imperfect channel state information on the detection performance of our proposed detectors are of interest. Another future topic of interest is channel coding for quantized reception and the exploitation of soft information available due to oversampling in the decoding process.

REFERENCES

- [1] C. Forsch, P. Zillmann, O. Alrabadi, S. Brueck, and W. Gerstacker, "Performance analysis of 1-bit quantization with oversampling for higher-order constellations," in *Proc. of IEEE Latin-American Conference on Communications (LATINCOM)*, 2022, pp. 1–6.
- [2] I. F. Akyildiz, A. Kak, and S. Nie, "6G and beyond: The future of wireless communications systems," *IEEE Access*, vol. 8, pp. 133 995–134 030, 2020.
- [3] B. Murmann, "The race for the extra decibel: A brief review of current ADC performance trajectories," *IEEE Solid-State Circuits Magazine*, vol. 7, no. 3, pp. 58–66, 2015.
- [4] J. Singh, O. Dabeer, and U. Madhow, "On the limits of communication with low-precision analog-to-digital conversion at the receiver," *IEEE Transactions on Communications*, vol. 57, no. 12, pp. 3629–3639, 2009.
- [5] E. Gilbert, "Increased information rate by oversampling," *IEEE Transactions on Information Theory*, vol. 39, no. 6, pp. 1973–1976, 1993.
- [6] S. Shamai, "Information rates by oversampling the sign of a bandlimited process," *IEEE Transactions on Information Theory*, vol. 40, no. 4, pp. 1230–1236, 1994.
- [7] T. Koch and A. Lapidoth, "Increased capacity per unit-cost by oversampling," in *Proc. of IEEE 26-th Convention of Electrical and Electronics Engineers in Israel*, 2010, pp. 000 684–000 688.
- [8] W. Zhang, "A general framework for transmission with transceiver distortion and some applications," *IEEE Transactions on Communications*, vol. 60, no. 2, pp. 384–399, 2012.
- [9] O. Dabeer, J. Singh, and U. Madhow, "On the limits of communication performance with one-bit analog-to-digital conversion," in *Proc. of IEEE 7th Workshop on Signal Processing Advances in Wireless Communications*, 2006, pp. 1–5.
- [10] S. Krone and G. Fettweis, "Achievable rate with 1-bit quantization and oversampling at the receiver," in *Proc. of IEEE Communication Theory Workshop*, 2010, pp. 1–2.
- [11] —, "Capacity of communications channels with 1-bit quantization and oversampling at the receiver," in *Proc. of 35th IEEE Sarnoff Symposium*, 2012, pp. 1–7.
- [12] —, "Communications with 1-bit quantization and oversampling at the receiver: Benefiting from inter-symbol-interference," in *Proc. of IEEE 23rd International Symposium on Personal, Indoor and Mobile Radio Communications - (PIMRC)*, 2012, pp. 2408–2413.

- [13] L. T. N. Landau, M. Dörpinghaus, and G. P. Fettweis, "1-bit quantization and oversampling at the receiver: Sequence-based communication," *EURASIP Journal on Wireless Communications and Networking*, vol. 2018, no. 1, Apr. 2018.
- [14] S. Jacobsson, G. Durisi, M. Coldrey, U. Gustavsson, and C. Studer, "One-bit massive MIMO: Channel estimation and high-order modulations," in *Proc. of IEEE International Conference on Communications Workshops (ICCW)*, 2015, pp. 1304–1309.
- [15] J. Zhang, L. Dai, S. Sun, and Z. Wang, "On the spectral efficiency of massive MIMO systems with low-resolution ADCs," *IEEE Communications Letters*, vol. 20, no. 5, pp. 842–845, 2016.
- [16] S. Jacobsson, G. Durisi, M. Coldrey, U. Gustavsson, and C. Studer, "Throughput analysis of massive MIMO uplink with low-resolution ADCs," *IEEE Transactions on Wireless Communications*, vol. 16, no. 6, pp. 4038–4051, 2017.
- [17] T. Halsig, L. Landau, and G. Fettweis, "Spectral efficient communications employing 1-bit quantization and oversampling at the receiver," in *Proc. of IEEE 80th Vehicular Technology Conference (VTC2014-Fall)*, 2014, pp. 1–5.
- [18] U. Ugurlu and R. Wichman, "Enabling low-resolution ADC with high-order modulations for millimeter-wave systems," in *Proc. of IEEE International Conference on Communications (ICC)*, 2016, pp. 1–6.
- [19] B. Sun, Y. Zhou, J. Yuan, Y.-F. Liu, L. Wang, and L. Liu, "High order PSK modulation in massive MIMO systems with 1-bit ADCs," *IEEE Transactions on Wireless Communications*, vol. 20, no. 4, pp. 2652–2669, 2021.
- [20] J. Choi, D. J. Love, D. R. Brown, and M. Boutin, "Quantized distributed reception for MIMO wireless systems using spatial multiplexing," *IEEE Transactions on Signal Processing*, vol. 63, no. 13, pp. 3537–3548, 2015.
- [21] S. Wang, Y. Li, and J. Wang, "Multiuser detection in massive MIMO with quantized phase-only measurements," in *Proc. of IEEE International Conference on Communications (ICC)*, 2015, pp. 4576–4581.
- [22] J. Choi, J. Mo, and R. W. Heath, "Near maximum-likelihood detector and channel estimator for uplink multiuser massive MIMO systems with one-bit ADCs," *IEEE Transactions on Communications*, vol. 64, no. 5, pp. 2005–2018, 2016.
- [23] S.-N. Hong, S. Kim, and N. Lee, "A weighted minimum distance decoding for uplink multiuser MIMO systems with low-resolution ADCs," *IEEE Transactions on Communications*, vol. 66, no. 5, pp. 1912–1924, 2018.
- [24] A. B. Üçüncü, E. Björnson, H. Johansson, A. Ö. Yılmaz, and E. G. Larsson, "Performance analysis of quantized uplink massive MIMO-OFDM with oversampling under adjacent channel interference," *IEEE Transactions on Communications*, vol. 68, no. 2, pp. 871–886, 2020.
- [25] Y. Nakashima, T. Yamazato, Y. Tadokoro, and S. Arai, "A stochastic resonance receiver for 4-PAM signals," in *Proc. of IEICE International Symposium on Nonlinear Theory and Its Applications (NOLTA2017)*, 2017, pp. 291–294.
- [26] Y. Nakashima, T. Yamazato, S. Arai, H. Tanaka, and Y. Tadokoro, "Noise-aided demodulation with one-bit comparator for multilevel pulse-amplitude-modulated signals," *IEEE Wireless Communications Letters*, vol. 7, no. 5, pp. 848–851, 2018.
- [27] P. Neuhaus, M. Dörpinghaus, H. Halbauer, S. Wesemann, M. Schlüter, F. Gast, and G. Fettweis, "Sub-THz wideband system employing 1-bit quantization and temporal oversampling," in *Proc. of IEEE International Conference on Communications (ICC)*, 2020, pp. 1–7.
- [28] D. He, Z. Wang, T. Q. S. Quek, S. Chen, and L. Hanzo, "Deep learning-assisted Terahertz QPSK detection relying on single-bit quantization," *IEEE Transactions on Communications*, vol. 69, no. 12, pp. 8175–8187, 2021.
- [29] Y. Zhang, D. Li, D. Qiao, and L. Zhang, "Analysis of indoor THz communication systems with finite-bit DACs and ADCs," *IEEE Transactions on Vehicular Technology*, vol. 71, no. 1, pp. 375–390, 2022.
- [30] X. Cheng, B. Xia, K. Xu, and S. Li, "Bayesian channel estimation and data detection in oversampled OFDM receiver with low-resolution ADC," *IEEE Transactions on Wireless Communications*, vol. 20, no. 9, pp. 5558–5571, 2021.
- [31] H. Sarrideen, M.-S. Alouini, and T. Y. Al-Naffouri, "An overview of signal processing techniques for Terahertz communications," *Proceedings of the IEEE*, vol. 109, no. 10, pp. 1628–1665, 2021.
- [32] J. M. Jornet and I. F. Akyildiz, "Channel modeling and capacity analysis for electromagnetic wireless nanonetworks in the Terahertz band," *IEEE Transactions on Wireless Communications*, vol. 10, no. 10, pp. 3211–3221, 2011.
- [33] B. Wang, F. Gao, S. Jin, H. Lin, and G. Y. Li, "Spatial- and frequency-wideband effects in millimeter-wave massive MIMO systems," *IEEE Transactions on Signal Processing*, vol. 66, no. 13, pp. 3393–3406, 2018.
- [34] I.-S. Kim and J. Choi, "Spatial wideband channel estimation for mmWave massive MIMO systems with hybrid architectures and low-resolution ADCs," *IEEE Transactions on Wireless Communications*, vol. 20, no. 6, pp. 4016–4029, 2021.
- [35] E. Vlachos, A. Kaushik, and M. Z. Shaker, "Millimeter wave channel estimation for lens based hybrid MIMO with low resolution ADCs," in *Proc. of IEEE International Conference on Communications Workshops (ICC Workshops)*, 2023, pp. 1789–1793.
- [36] A. Doshi and J. G. Andrews, "One-bit mmWave MIMO channel estimation using deep generative networks," *IEEE Wireless Communications Letters*, vol. 12, no. 9, pp. 1593–1597, 2023.
- [37] T. Mewes, S. Zeitz, P. Neuhaus, M. Dörpinghaus, and G. Fettweis, "Channel estimation for two-wave with diffuse power fading channels under 1-bit quantization," in *Proc. of IEEE Wireless Communications and Networking Conference (WCNC)*, 2023, pp. 1–6.
- [38] A. Mezghani and J. A. Nossek, "How to choose the ADC resolution for short range low power communication?" in *Proc. of IEEE International Symposium on Circuits and Systems*, 2010, pp. 1025–1028.
- [39] S. Krone and G. Fettweis, "Energy-efficient A/D conversion in wideband communications receivers," in *Proc. of IEEE Vehicular Technology Conference (VTC2011-Fall)*, 2011, pp. 1–5.
- [40] P. Neuhaus, M. Schlüter, C. Jans, M. Dörpinghaus, and G. Fettweis, "Enabling energy-efficient Tbit/s communications by 1-bit quantization and oversampling," in *Proc. of Joint European Conference on Networks and Communications & 6G Summit (EuCNC/6G Summit)*, 2021, pp. 84–89.
- [41] O. Castañeda, S. H. Mirfarshbafan, S. Ghajari, A. Molnar, S. Jacobsson, G. Durisi, and C. Studer, "Resolution-adaptive all-digital spatial equalization for mmWave massive MU-MIMO," in *Proc. of IEEE 22nd International Workshop on Signal Processing Advances in Wireless Communications (SPAWC)*, 2021, pp. 386–390.
- [42] R. Walden, "Analog-to-digital converter survey and analysis," *IEEE Journal on Selected Areas in Communications*, vol. 17, no. 4, pp. 539–550, 1999.
- [43] B. Murmann, "ADC performance survey 1997-2022." [Online]. Available: <http://web.stanford.edu/~murmanc/adcsurvey.html>
- [44] W. Feller, *An Introduction to Probability Theory and Its Applications*, 3rd ed. John Wiley & Sons, 1968, vol. 1.
- [45] T. M. Cover and J. A. Thomas, *Elements of Information Theory*, 2nd ed. John Wiley & Sons, 2006.
- [46] A. Moldovan, M. A. Ruder, I. F. Akyildiz, and W. H. Gerstacker, "LOS and NLOS channel modeling for terahertz wireless communication with scattered rays," in *Proc. of IEEE Globecom Workshops (GC Wkshps)*, 2014, pp. 388–392.
- [47] R. Piesiewicz, C. Jansen, D. Mittleman, T. Kleine-Ostmann, M. Koch, and T. Kurner, "Scattering analysis for the modeling of THz communication systems," *IEEE Transactions on Antennas and Propagation*, vol. 55, no. 11, pp. 3002–3009, 2007.
- [48] L. John, A. Tessmann, A. Leuther, P. Neining, T. Merkle, and T. Zwick, "Broadband 300-GHz power amplifier MMICs in InGaAs mHEMT technology," *IEEE Transactions on Terahertz Science and Technology*, vol. 10, no. 3, pp. 309–320, 2020.
- [49] S. Priebe, M. Jacob, and T. Kürner, "The impact of antenna directivities on THz indoor channel characteristics," in *Proc. of 6th European Conference on Antennas and Propagation (EUCAP)*, 2012, pp. 478–482.